Available online at www.sciencedirect.com
ScienceDirect
Trans. Nonferrous Met. Soc. China 26(2016) 2754−2761
Transactions of Nonferrous Metals Society of China
www.tnmsc.cn

Two-step sintering of magnesium aluminate spinels and their corrosion in Na_3AlF_6−AlF_3−CaF_2−Al_2O_3 bath

Jian-hua LIU, Xiao-jun LÜ, Jie LI, Ling-yun HU, Liang-xing JIANG

School of Metallurgy and Environment, Central South University, Changsha 410083, China

Received 1 December 2015; accepted 18 May 2016

Abstract: New types of refractory materials need to be developed for designing the man-made ledge of the Hall−Héroult cell for aluminum electrolysis, which are currently constructed by frozen ledge. Magnesium aluminate spinel (MAS) as potential candidate materials was prepared by two-step sintering. The densification and grain growth of the MAS were investigated by the Archimedes drainage method and scanning electron microscope (SEM). All the specimens were corroded in a Na_3AlF_6−AlF_3−CaF_2−Al_2O_3 bath to assess the corrosion resistance. The results show that a MAS material with a high relative density of 99.2% and a homogeneous microstructure is achieved under two-step sintering conditions. The corrosion mechanisms of MAS in Na_3AlF_6−AlF_3−CaF_2−Al_2O_3 bath are mainly proposed by dissolution of MAS, formation of aluminum oxide, and diffusion of fluorides. The MAS prepared by two-step sintering exhibits good corrosion resistance to the Na_3AlF_6−AlF_3−CaF_2−Al_2O_3 bath.

Key words: magnesium aluminate spinel; sintering; aluminum electrolysis; corrosion resistance

1 Introduction

At present, Si_3N_4-bonded SiC sidewall materials that are used in Hall−Héroult cells rely on the formation of a solid cryolite ledge to prevent corrosive electrolyte attack [1]. The frozen ledge will be dissolved when the anode effect occurs. In this case, sidewalls will be directly exposed to the corrosive electrolyte, thereby significantly reducing the lifetime of the Si_3N_4-bonded SiC sidewall materials [2]. In addition, the quality of the dissolved solid ledge will be difficult to measure, which results in the distortion of point feeding and the failure of analytical methods based on mass balance. Driven by the need to replace the frozen ledge, we proposed man-made ledge materials used in the Hall−Héroult cells in our previous study to overcome these disadvantages of the frozen ledge [3,4]. One of the primary obstacles to the implementation of this idea is the lack of a suitable material that can withstand the attack of corrosive electrolyte.

Recent work on the corrosion of nickel ferrite spinel in cryolite demonstrates the suitability of the material as an alternative sidewall refractory [5,6]. NIGHTINGALE et al [5] tested the corrosion resistance of nickel ferrite to a cryolite-based bath and reported that nickel ferrite spinel demonstrated good resistance to dissolution in cryolite-based bath. The main potential weakness of nickel ferrite is the possibility of contamination of the molten aluminum product. Magnesium aluminate spinel (MAS) has been widely reported as refractory applications in metallurgical and other high temperature process industries [7]. MAS may be suitable for use in bath zones because of its high stability in the molten bath. YAN et al [8] studied the corrosion of MAS in electrolyte melts at 980 °C. The results indicated that MAS exhibits good corrosion resistance towards the melts. Moreover, the application of MAS would not contaminate aluminum melt. Unfortunately, MAS cannot be densified though single-stage firing because MAS formation is accompanied by 5% to 7% volume expansion [9,10]. Insufficient density of MAS results in decline of corrosion resistance. Thus, a double-stage firing process was used as the densification of MAS [11]. In the first stage, the reactant oxides (alumina and magnesia) are converted to spinel. Then, MAS compacts are sintered at the high temperature in the second stage.

So far many research works have been carried out to

Foundation item: Project (51374240) supported by the National Natural Science Foundation of China; Project (2012BAE08B02) supported by the National Science and Technology Pillar Program of China

Corresponding author: Xiao-jun LÜ; Tel: +86-731-88830649; E-mail: csuxiaojun@126.com

DOI: 10.1016/S1003-6326(16)64405-9

improve the sintering behavior of MAS by sintering aids [12−14]. In addition, other sintering methods such as spark plasma sintering [15], microwave sintering [16], and hot pressing sintering [17] are used to replace conventional methods. However, the complexity and expensiveness of these methods restrict their industrial applications. Therefore, a relatively simple and effective method is desired to improve the densification and corrosion resistance of MAS. One of the sintering methods which are capable of fabricating dense structure as well as a homogeneous microstructure is two-step sintering. This novel method was introduced by CHEN and WANG [18]. In the first step of two-step sintering, the specimen is kept at a higher temperature (T_1) for a short time to reach a critical density and then rapidly cooled down to lower temperature (T_2) and soaked for a relatively prolonged time for densification without grain growth [19]. However, there are almost no reports about two-step sintering of MAS.

In this work, the feasibility of two-step sintering of MAS was investigated. Moreover, corrosion resistance of MAS produced by conventional sintering and two-step sintering was studied and compared.

2 Experimental

2.1 Sintering of MAS specimens

Stoichiometric MAS powders were synthesized at 1200 °C for 3 h by a conventional solid state reaction method using MgO and Al_2O_3 with more than 99% purity as raw materials. MAS powder mixture was planetary ball-milled for 10 h with zirconia balls using ethanol media. The average particle size of MAS powder was 1.8 μm. Milled powders were uniaxially pressed into cuboid specimens with the dimensions of 60 mm × 15 mm × 10 mm at 200 MPa on a hydraulic press (WE–300C). Sintering of the specimens was carried out through conventional sintering (CS) and two-step sintering (TSS) methods. The sintered specimens were termed as CS and TSS, respectively.

Conventional sintering was carried out in air at a peak temperature (T) with a heating rate of 3 °C/min. These specimens were held at the peak temperature for 10 h and then the furnace was cooled down to room temperature. Two preliminary sintering tests were undergone to determine the sintering parameters of two-step sintering. One test consisted of a single-step sintering (SSS) which was used to determine T_1 of the two-step sintering. In this test, the SSS was carried out at 1400−1750 °C (T_1) in air with 50 °C temperature intervals. The specimens were heated to the maximum temperature (T_1) without any holding time and then cooled down to room temperature. Linear shrinkage data were calculated by comparing the diameters of sintered specimens. The linear shrinkage rate was obtained by differentiating the measured linear shrinkage data. Another test was carried out by the two-step sintering. The heating rates were 10 and 5 °C/min below and above 1400 °C, respectively. The specimens were then cooled to a lower temperature T_2 at 30 °C/min and held for isothermal sintering with a holding time of 10 h. Time and temperature conditions as well as heating and cooling rates in conventional sintering and two-step sintering procedures are compared in Fig. 1.

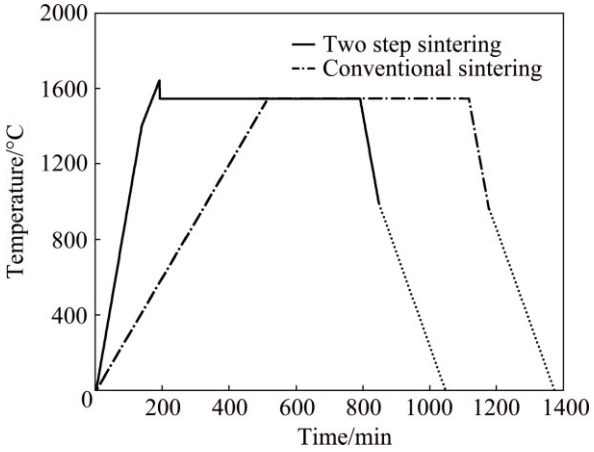

Fig. 1 Time–temperature profile of conventional sintering and two-step sintering

2.2 Corrosion tests

Corrosion of MAS in the Na_3AlF_6−AlF_3−CaF_2−Al_2O_3 bath was studied in this work. The electrolyte was prepared from reagent grade Na_3AlF_6, AlF_3, CaF_2, and $A1_2O_3$. Compositions were 79.8% Na_3AlF_6, 12.2% AlF_3, 5% CaF_2, and 3% $A1_2O_3$. The electrolytic liquidus temperature is 953 °C. The CS and TSS specimens were placed into a graphite crucible with electrolyte and were then held at 970 °C. After a certain amount of corrosion time (3, 6, 9, and 12 h), the specimens were taken out from bath. After naturally cooling to room temperature, the corroded specimens were placed in a 30% aluminum chloride solution and maintained at 80 °C for 4 h to remove the electrolyte. To further eliminate the electrolyte, the specimens were immersed in boiling water for 5 h and then finally dried overnight at 120 °C. An electronic balance (TP−5000E) was used to measure the quality of the specimens before and after corrosion. The cross-sections of corroded specimens were prepared by perpendicularly cutting and polishing with different grades of SiC abrasive papers.

2.3 Characterization

The bulk density and apparent porosity of the sintered products were measured by using the conventional liquid displacement method, which applied Archimedes' principle. Phase analysis was done by

X-ray diffraction technique (by Rigaku3014). Microstructures of the sintered products were observed with a scanning electron microscope (SEM, Nova NanoSEM 230) using sputtered gold coating on the polished surface after thermal etching. Quantitative elemental analysis of the selected grain was done by EDAX. Grain size of samples sintered under CS, SSS and TSS heating regimes was determined by the linear intercept method in SEM micrographs [20].

3 Results and discussion

3.1 Two preliminary sintering tests

The linear shrinkage and linear shrinkage rate of the MAS specimens as a function of temperature are shown in Fig. 2, where ΔL is defined as the difference between the diameter of the samples before and after sintering; Lo is the diameter of the samples before sintering. The absolute value of linear shrinkage rate, identifying with densification rate, increases with sintering temperature from 1400 to 1650 °C and decreases sharply from 1650 to 1750 °C. The amount of shrinkage at 1650 °C is 8.34%. Based on Ref. [21], the exhausting of densification rate is associated with the final sintering stage or the coarsening of the grain size. In this case, an obvious grain growth is observed when the sintering temperature is higher than 1650°C corresponding to the decrease of the densification rate. It is known that the grain growth increases the diffusion distance and makes the sintering become difficult. Since the state of the specimen after the first step sintering critically affects the subsequent second step, the grain growth resulted from over-heating must be cautiously avoided. Accordingly, the appropriate temperature T_1 is set at 1650 °C where the densification rate shows the highest value throughout a single step sintering, and the corresponding relative density is 93.77% of the theoretical density (TD).

The effect of sintering temperature on the relative density and apparent porosity of the MAS compacts sintered in the temperature range of 1400−1750 °C without any holding time is shown in Fig. 3. The specimens start to exhibit densification at temperatures higher than 1400 °C. The relative density increases from 66.2% to 98.02% TD with increasing sintering temperature. The apparent porosity decreases from 34.44% to 0 with increasing sintering temperature.

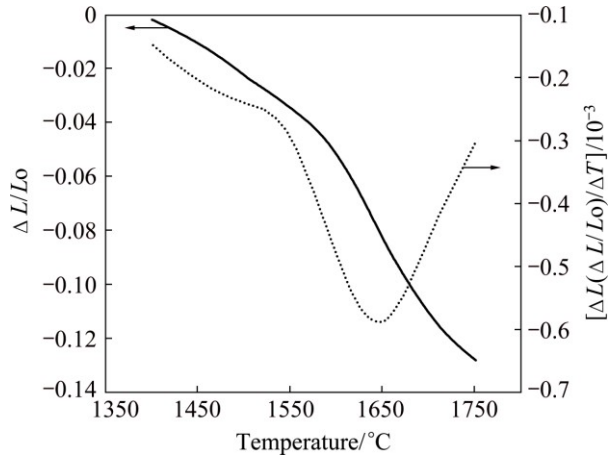

Fig. 2 Shrinkage and shrinkage rate profile of MAS specimens

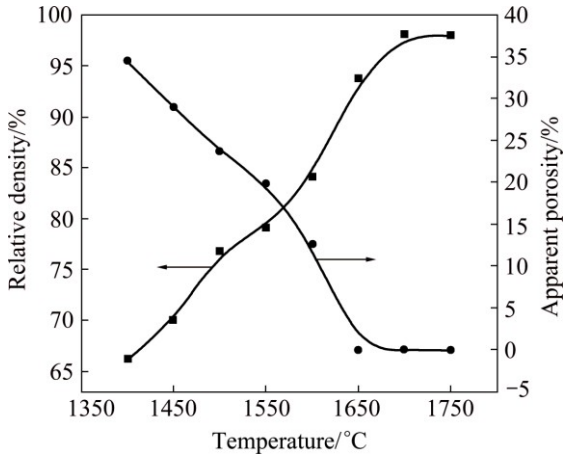

Fig. 3 Variation of relative density and apparent porosity of MAS specimens sintered in temperature range of 1400−1750 °C without any holding time

The effect of sintering temperature on the relative density and grain growth of the MAS compacts sintered in the temperature range of 1400−1750 °C without any holding time is shown in Fig. 4. The specimens start to exhibit densification at temperatures higher than 1400 °C. Figure 4 shows that the relative density increases significantly from 84.08% to 93.77% TD and the average grain size increases from 3.52 to 4.93 μm with increasing temperature from 1600 to 1650 °C. Densification is accelerated without significant grain growth in the temperature range of 1600−1650 °C. When the sintering temperature is higher than 1650 °C, an obvious grain growth is observed, and this growth corresponds to the

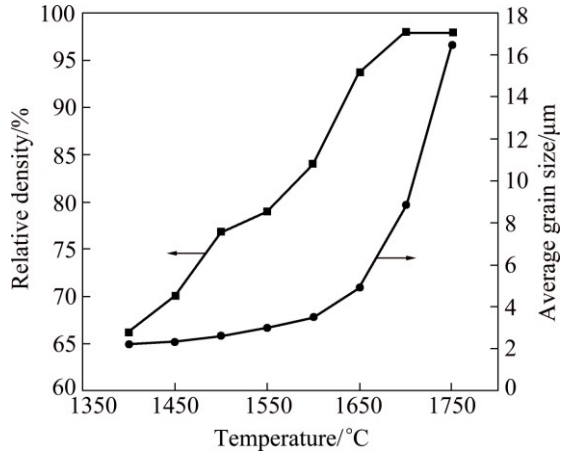

Fig. 4 Relative density and average grain size of MAS specimens after SSS

decrease of the densification rate. For example, when the relative density increases from 93.77% to 98.02% TD with the increasing temperature from 1650 to 1700 °C, the average grain size becomes coarser (from 4.93 to 8.87 μm). LI and YE [22] reported that the fast grain growth started at about 90% TD. Interestingly, ceramic sintering transits from intermediate-stage sintering (with a relative density of about 65%−90% TD) to the final-stage sintering during a pressureless sintering process at about 90% TD [23]. In intermediate-stage sintering, the pores can pin the grain boundary and hinder grain boundary migration, which in turn would suppress grain growth [24].

Above studies show that the densification kinetics of MAS compacts is different from grain growth kinetics. The densification and grain growth of the MAS compacts occur at different temperatures, indicating the possibility of enhancing dense ceramics without promoting rapid grain growth.

Although a higher relative density product (98.02% TD) can be obtained, the densification of these powders is often accompanied by the forming of non-uniform microstructures. To obtain MAS with a high relative density and a homogeneous microstructure, a two-step sintering method was used to prepare the MAS. Based on the SSS tests mentioned in the previous section, the densification rate shows the highest value at 1650 °C. Moreover, with increasing sintering temperature from 1600 to 1650 °C, the relative density of MAS increases rapidly, and the average grain size of the MAS compacts increases slowly, fast grain growth occurs at above 1650 °C. Thus, the appropriate temperature T_1 is set at 1650 °C. Moreover, the choice for T_2 needs to be considered because an undesired grain growth may be generated when the T_2 is higher. An incomplete densification is attained owing to the insufficiency of grain boundary diffusion. Previous successful experiences for TSS exhibit that T_2 should be lower than T_1 with a gap of 50−150 °C [16,20]. Hence, the temperature range of the second-step sintering (T_2) is 50−150 °C lower than T_1. Thus, the temperature used in the second step was 1550 °C in this work.

Average grain size and relative density (apparent porosity) of the sintered specimens play important roles in controlling the corrosion resistance of ceramic materials. Uniform grain size distribution and a pore-free microstructure would be beneficial for obtaining a better corrosion resistance. In order to highlight the effect of two-step sintering regime, the average grain size versus relative density curves of both SSS and the successful two-step sintering experiment are depicted in Fig. 5. Figure 5 shows that a higher relative density (99.2% TD) of the MAS specimens is obtained and grain growth is suppressed during the second-step sintering.

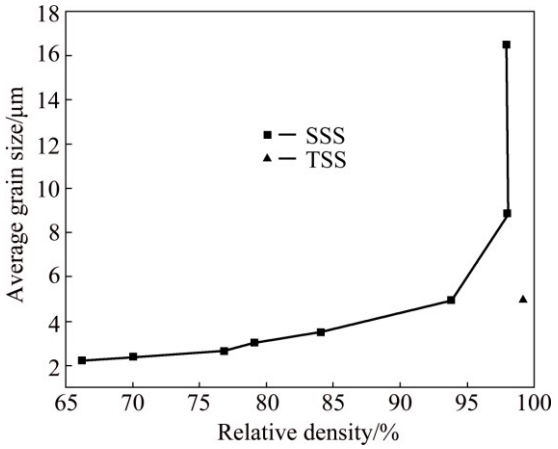

Fig. 5 Average grain size versus relative density of MAS specimens sintered by SSS and TSS

The SEM images of MAS specimens sintered under the two-step sintering and conventional sintering are shown in Fig. 6. Conventional sintering is carried out in air at 1550 °C with a holding time of 10 h and a heating rate of 3 °C/min. The relative density and apparent porosity of CS are 98.5% and 0.2%, respectively. Figure 6(b) shows that exaggerated grain growth in the conventional sintered specimen results in an uneven grain size distribution. As shown in Fig. 6(a), compared with the conventional sintering, the microstructure of MAS sintered at two-step sintering is more compact with very few pores. A material with a higher relative density and a more homogeneous microstructure is obtained by the second-step sintering which might slow down the penetration of the electrolyte.

3.2 Corrosion test

To understand the behavior of the magnesium aluminate spinels in a cryolite-based bath, isopleths are calculated by using the thermodynamic software FactSage 6.2. In these calculations, the composition is varied from the bath composition to magnesium aluminate spinels at a constant pressure. The isopleths are phase stability diagrams that represent the pseudo-binary section taken across temperature–composition space.

The cryolite-based bath and magnesium aluminate spinels are noted as “bath” and $MgAl_2O_4$ in Fig. 7, respectively. The diagram can be seen as a eutectic between bath and $MgAl_2O_4$. The phases for each field are given in Fig. 7. For the temperatures of interest (950−1000 °C), liquid bath, $NaMgF_3$, Al_2O_3, and spinel are observed. The bath phase has a variable composition and is different to the input “bath”. The presence of spinel phase in the majority of phase field indicates that there is limited solubility of the spinel (magnesium aluminate) in the bath.

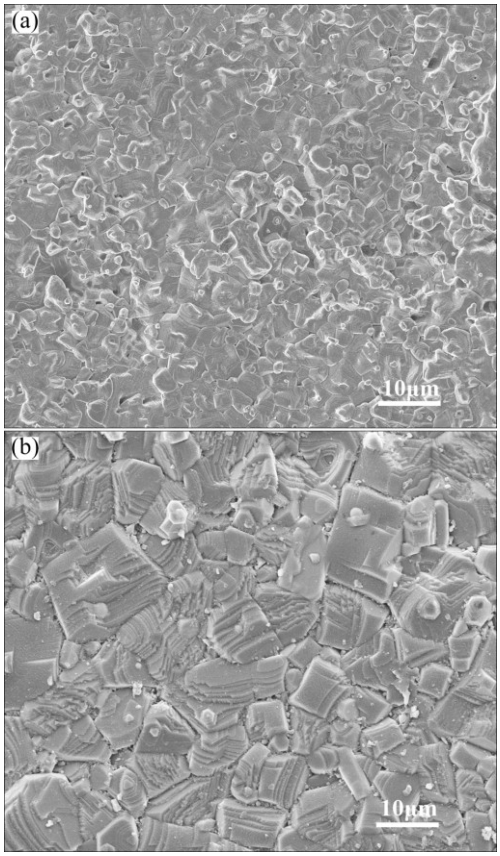

Fig. 6 SEM images of MAS specimens sintered by TSS (a) and CS (b)

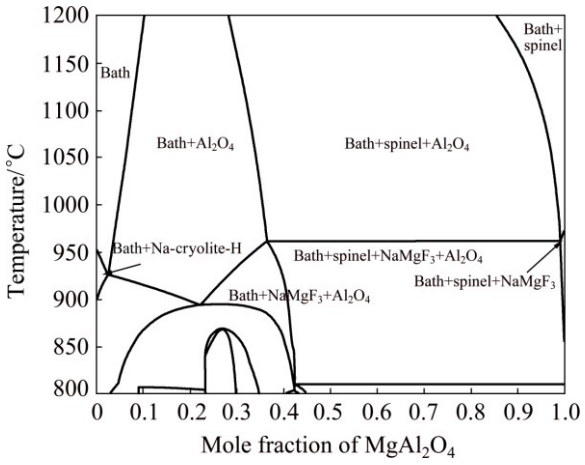

Fig. 7 Bath and $MgAl_2O_4$ isopleth calculated at constant pressure of 1×10^{-5} Pa

At the bath-rich end of the system, isopleths show the formation of Al_2O_3 phase. Na−cryolite−H is formed at low temperature levels and the bath-rich end of the system. At the $MgAl_2O_4$-rich end of the system, Al_2O_3 and $NaMgF_3$ are formed. As expected, no metal formation is found under the system.

Figure 8 shows the cross-section morphologies of the CS and TSS specimens after corrosion tests at 970 °C for 3 h. The corroded specimens are termed as CS3 and TSS3, respectively. After corrosion test, the thicknesses of the residual corrosion layer formed on CS (Fig. 8(a)) and TSS (Fig. 8(b)) specimens in the molten electrolyte are 1.32 mm and 0.51 mm, respectively. The residual corrosion layer of CS3 can be divided into two regions of a porous layer and a dense layer, and no visible porous layer is found in the residual corrosion layer of TSS3. The corrosion layer is mainly composed of columnar crystal materials and solid particles. The mass gains are 8.86% and 0.45%, respectively. At the initial stage of the corrosion, the mass gain may be due to the permeation of electrolyte. In addition, the high apparent porosity (0.2%) and the amount of small grain of the CS specimen cause the electrolyte to permeate easily and react with the small grain.

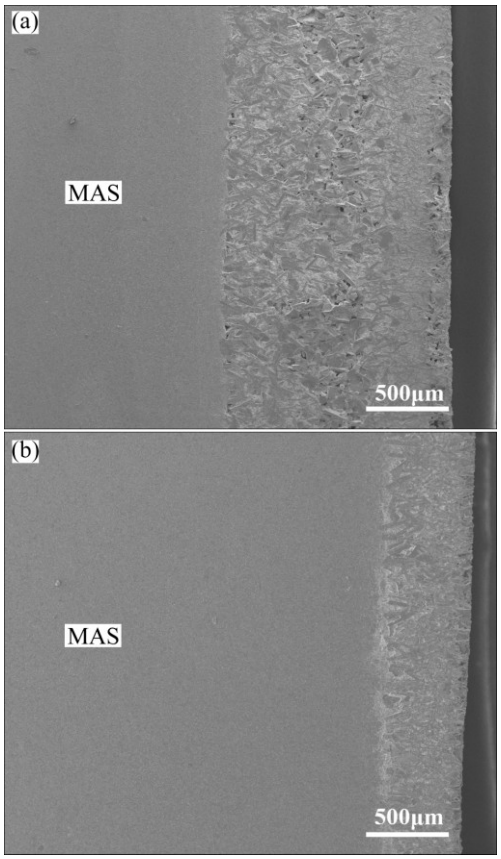

Fig. 8 Cross-section morphologies of CS (a) and TSS (b) specimens after corrosion tests at 970 °C for 3 h

Line scan analyses of O, F, Na, Mg, and Al across the interface from MAS to the corrosion layer and the EDS analysis of special points after corrosion tests at 970 °C for 3 h are shown in Fig. 9. Figure 9(a) indicates that the Mg content shows a sharp decline across the interface from MAS matrix to the corrosion layer. In addition, the variation tendency of Mg content among corrosion layers is similar to that of F and Na contents, and the variation tendency in Al content is similar to that of O content. Figure 9(b) shows that the elemental compositions of the grain in the solid particle are F, Na,

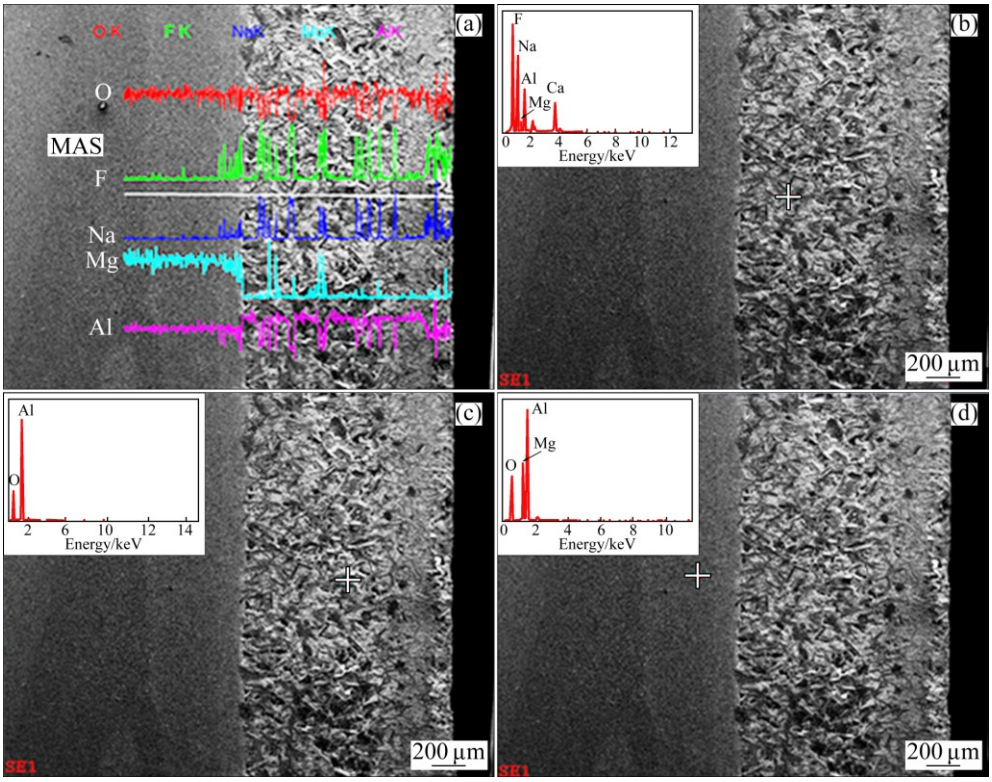

Fig. 9 Line scan analyses of O, F, Na, Mg, and Al across interface from MAS to corrosion layer (a) and EDS analyses of special points ((b), (c), (d)) after corrosion test at 970 °C for 3 h

Mg, Ca, and Al, thereby indicating that the electrolyte penetrates into the surface layer of MAS and reacts with MAS. It can be observed in Fig. 9(c) that the corrosion process occurs, and columnar crystal material (Al_2O_3) is one of the corrosion products. Figure 9(d) shows that the elemental compositions of the grain in MAS matrix are O, Mg, and Al, and the material is identified as $MgAl_2O_4$.

To understand the corrosion mechanisms of the MAS specimens in the electrolyte, phase identification of MAS specimens surfaces before and after corrosion test was analyzed by XRD (Fig. 10). Combined with the results of the previous sections, results reveal that the major new materials are corundum and fluoride, which are formed via the reactions (1) and (2). However, fluorides on the surface of corroded specimen are washed by aluminum chloride solution.

$$3MgAl_2O_4+2Na_3AlF_6=4Al_2O_3+3NaF+3NaMgF_3 \quad (1)$$

$$3MgAl_2O_4+2AlF_3=4Al_2O_3+3MgF_2 \quad (2)$$

Based on the above-mentioned, the corrosion mechanisms of MAS in Na_3AlF_6−AlF_3−CaF_2−Al_2O_3 bath are mainly proposed by dissolution of MAS, formation of aluminum oxide, and the diffusion of fluorides.

The high-porosity MAS specimens prepared via conventional sintering show more severer bath infiltration. However, the materials obtained by two-step sintering

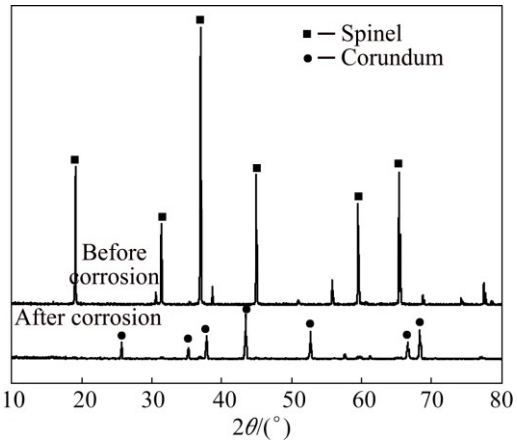

Fig. 10 XRD patterns of MAS specimens surface before and after corrosion test

possess a dense structure with improved corrosion resistance. For example, for the CS specimens, the corrosion layers are 1.32, 1.4, 1.52, and 1.73 mm in thickness with the corrosion time of 3, 6, 9, and 12 h, respectively. By contrast, for the TSS specimens, the corrosion layer thicknesses are only 0.51, 0.62, 0.7, and 0.82 mm, respectively. These results indicate that the TSS specimens probably possess even higher chemical stability than CS specimens in the molten electrolyte. This difference is due to the high relative density and a homogeneous microstructure of MAS, which can be

obtained by two-step sintering. The electrolyte permeates easily into the MAS matrix because of the high porosity. In addition, small grains are more likely to be corroded. Thus, large grains fall off easily despite being partially dissolved.

4 Conclusions

1) This work verifies the possibility of producing dense MAS without promoting rapid grain growth by controlling the first and second step sintering temperatures of two-step sintering due to different temperatures of densification and grain growth. Temperature T_1 for the first step of sintering should be set at 1650 °C, which corresponds to the interplay between the average grain size and densification rate of MAS compacts. The two-step sintering condition (T_1=1650 °C, 0 h and T_2=1550 °C, 10 h) is selected, because densification is accelerated without significant grain growth. The relative density and apparent porosity of MAS sintered under optimum two-step sintering are 99.2% TD and 0, respectively.

2) The corrosion mechanism of MAS in Na_3AlF_6−AlF_3−CaF_2−Al_2O_3 bath is complex, involving dissolution of MAS, formation of aluminum oxide, and diffusion of fluorides. The MAS specimens exhibit good corrosion resistance to dissolution in the Na_3AlF_6−AlF_3−CaF_2−Al_2O_3 bath owing to their high density and homogeneous microstructure.

References

[1] SONNTAG A. New R-SiC extends service life in kiln furniture [J]. American Ceramic Society Bulletin, 1997, 76(11): 51−54.

[2] QIU Z X. Aluminum smelting by pre-baked slot [M]. 3rd ed. Beijing: Metallurgy Industry Press, 2005: 506. (in Chinese)

[3] LÜ Xiao-jun, LAI Yan-qing, ZHANG Chao, LI Jie. A man-made ledge aluminum electrolytic cell: China Patent, 103060848A [P]. 2013−04−24. (in Chinese)

[4] LÜ X J, ZHANG C, LAI Y Q, TIAN Z L, JIA M, LI J. Al_2O_3−Na_3AlF_6 man-made ledge composites for aluminum electrolysis cells [C]//Light Metals. San Diego: John Wiley & Sons, Inc, 2014: 615−619.

[5] NIGHTINGALE S A, LONGBOTTOM R J, MONAGHAN B J. Corrosion of nickel ferrite refractory by Na_3AlF_6−AlF_3−CaF_2−Al_2O_3 bath [J]. Journal of the European Ceramic Society, 2013, 33(13): 2761−2765.

[6] XU Y, LI Y, SANG S, REN B, QIN Q, YANG J. Preparation of MgO−$NiFe_2O_4$−TiO_2 materials and their corrosion in Na_3AlF_6−AlF_3−K_3AlF_6 bath [J]. Ceramics International, 2014, 40(8): 13169−13177.

[7] GHOSH C, GHOSH A, HALDAR M K. Studies on densification, mechanical, micro-structural and structure–properties relationship of magnesium aluminate spinel refractory aggregates prepared from Indian magnesite [J]. Materials Characterization, 2015, 99: 84−91.

[8] YAN X Y, MUKHLIS R Z, RHAMDHAMI M A, BROOKS G. Aluminate spinels as sidewall linings for aluminum smelters [C]//Light Metals. San Diego: John Wiley & Sons, Inc, 2011: 1085−1090.

[9] RYSHKEWITCH E, RICHERSON D W. Oxide ceramics [M]. New York: Academic Press, 1960: 257−274.

[10] SARKAR R, DAS S K, BANERJEE G. Calcination effect on magnesium hydroxide and aluminium hydroxide for the development of magnesium aluminate spinel [J]. Ceramics International, 2000, 26(1): 25−28.

[11] LI J, LIU J H, LV X J, LAI Y Q. Effect of Sc_2O_3 addition on the densification and microstructure of different spinelized magnesium aluminate spinel [J]. Transactions of Nonferrous Metals Society of China, 2016, 26(1): 144−151.

[12] MROZ T, GOLDMAN L M, GLEDHILL A D, LI D, PADTURE N P. Nanostructured, infrared-transparent magnesium-aluminate spinel with superior mechanical properties [J]. International Journal of Applied Ceramic Technology, 2012, 9(1): 83−90.

[13] SUTORIK C, GILDE G, SWAB J J, COOPER C, GAMBLE R, SHANHOLTZ E. The production of transparent $MgAl_2O_4$ ceramic using calcined powder mixtures of $Mg(OH)_2$ and γ-Al_2O_3 or AlOOH [J]. International Journal of Applied Ceramic Technology, 2012, 9(3): 575−587.

[14] GANESH I. A review on magnesium aluminate ($MgAl_2O_4$) spinel: Synthesis, processing and applications [J]. International Materials Reviews, 2013, 58(2): 63−112.

[15] PELLIZZARI M, FEDRIZZI A, ZADRA M. Influence of processing parameters and particle size on the properties of hot work and high speed tool steels by spark plasma sintering [J]. Materials Design, 2011, 32(4): 1796−1805.

[16] SAVARY E, MARINEL S, COLDER H, HARNOIS F X, RETOUX R. Microwave sintering of nano-sized ZnO synthesized by a liquid route [J]. Powder Technology, 2011, 208(2): 521−525.

[17] TING C J, LU H Y. Hot-pressing of magnesium aluminate spinel—I. Kinetics and densification mechanism [J]. Acta Materialia, 1999, 47(3): 817−830.

[18] CHEN W, WANG X H. Sintering dense nanocrystalline ceramics without final-stage grain growth [J]. Nature, 2000, 404(6774): 168−171.

[19] WANG X H, CHEN P L, CHEN I W. Two-step sintering of ceramics with constant grain-size, I. Y_2O_3 [J]. Journal of the American Ceramic Society, 2006, 89(2): 431−437.

[20] WURST J C, NELSON J A. Lineal intercept technique for measuring grain size in two-phase polycrystalline ceramics [J]. Journal of the American Ceramic Society, 1972, 55(2): 109.

[21] SHI J L, GAO J H, LIN Z X, YAN D S. Effect of agglomerates in ZrO_2 powder compacts on microstructural development [J]. Journal of Materials Science, 1993, 28(2): 342−348.

[22] LI J G, YE Y P. Densification and grain growth of Al_2O_3 nanoceramics during pressureless sintering [J]. Journal of the American Ceramic Society, 2006, 89(1): 139−143.

[23] MAYO M J, HAGUE D C, CHEN D J. Processing nanocrystalline ceramics for applications in superplasticity [J]. Materials Science and Engineering A, 1993, 166(1): 145−159.

[24] SKANDAN G, HAHN H, RODDY M, CANNON W R. Ultrafine-grained dense monoclinic and tetragonal zirconia [J]. Journal of the American Ceramic Society, 1994, 77(7): 1706−1710.

两步烧结法制备镁铝尖晶石及其在 Na_3AlF_6−AlF_3−CaF_2−Al_2O_3 电解质中的腐蚀

刘建华，吕晓军，李 劼，胡凌云，蒋良兴

中南大学 冶金与环境学院，长沙 410083

摘 要：霍尔−埃鲁特铝电解槽需要一种新型的耐火材料来取代现有的凝固电解质构筑的炉帮。用两步烧结法制备的镁铝尖晶石作为潜在的候选材料，采用阿基米德排水法和扫描电镜研究镁铝尖晶石的致密化和晶粒长大。将所制备的试样在 Na_3AlF_6−AlF_3−CaF_2−Al_2O_3 电解质中腐蚀以评价其耐蚀性能。结果表明，用两步烧结法可制备高致密度(99.2%)和均匀显微结构的镁铝尖晶石。镁铝尖晶石对 Na_3AlF_6−AlF_3−CaF_2−Al_2O_3 电解质的腐蚀机理主要是镁铝尖晶石的溶解、氧化铝的形成和氟化物的扩散。两步烧结法制备的镁铝尖晶石具有良好的耐 Na_3AlF_6−AlF_3−CaF_2−Al_2O_3 电解质腐蚀性能。

关键词：镁铝尖晶石；烧结；铝电解；耐腐蚀性能

(Edited by Xiang-qun LI)